Fully coherent growth of Ge on free-standing Si(001) nanomesas

F. Montalenti,[1] M. Salvalaglio,[1] A. Marzegalli,[1] P. Zaumseil,[2] G. Capellini,[2,3,*] T. U. Schülli,[4] M. A. Schubert,[2] Y. Yamamoto,[2] B. Tillack,[2,5] and T. Schroeder[2,6]

[1]*L-NESS and Dipartimento di Scienza dei Materiali, Università di Milano-Bicocca, Via R. Cozzi 55, 20126 Milano, Italy*

[2]*IHP, Im Technologiepark 25, 15236 Frankfurt (Oder), Germany*

[3]*Dipartimento di Scienze, Università degli Studi Roma Tre, Viale G. Marconi 446, 00146 Roma, Italy*

[4]*ESRF, 38043 Grenoble, France*

[5]*Technische Universität Berlin, 10587 Berlin, Germany*

[6]*Brandenburgische Technische Universität Cottbus, 03046 Cottbus, Germany*

(Received 12 July 2013; revised manuscript received 9 December 2013; published 2 January 2014)

We investigate the structural properties of Ge nanostructures selectively grown on Si. Defect-free nanostructures with a lateral size of 100 nm and surrounded by a thick (∼20 times larger than the coherent-film limit) Ge layer are achieved as demonstrated by transmission electron microscopy. As demonstrated by modeling based on elasticity theory solved by finite element methods, the peculiar combination of morphology and chemical composition of the nanostructures allows for a very efficient elastic relaxation of the heteroepitaxial strain. We demonstrate that, despite the relatively large size of the nanostructures, even a single dislocation would raise the energy of the system. A direct comparison between the strain field predicted by modeling and measured by energy-dispersive synchrotron-radiation grazing incidence x-ray diffraction shows substantial agreement.

DOI: 10.1103/PhysRevB.89.014101 PACS number(s): 81.15.Gh, 62.25.−g, 68.55.A−

I. INTRODUCTION

Modern nanoscience and nanotechnology require us to theoretically understand and experimentally engineer materials on the atomic scale.[1] For example, the continuous down-scaling of transistor device dimensions on the mature silicon technology platform achieved a level of control which made it possible to "write in Si" the first chapter of the nanoelectronics success story. However, although Si integrated circuits (ICs) will also clearly dominate future information technology markets, fundamental limits in physical properties of silicon itself are met and must be overcome to further increase the performance and functionality of future nanoelectronics. The integration of alternative semiconductor materials with superior optoelectronic properties is thus an important materials science approach to make Si-based circuit technology better adjusted for future technology requirements. For example, sub-50 nm InGaAs-based *n*-channel[2,3] and Ge-based *p*-channel[4,5] field effect transistors are investigated for future complementary metal oxide semiconductor technology. Furthermore, III-V quantum dot[6,7] and tensile strained Ge[8,9] heterostructures are discussed as optical gain media for laser source integration on Si, thus enabling the convergence of photonics and electronics functions in integrated optoelectronics. Other applications are found in the nanoelectronic-biology frontier, where semiconductor nanowires on Si are used as links for building up active electronic interfaces with biological systems.[10] In all these applications, nanostructures of lattice mismatched semiconductors must be grown on Si substrates with appropriate quality materials to fully exploit their superior optoelectronics properties to increase device performance with respect to the "standard" Si technology.

Classical mismatched heteroepitaxy of planar films unavoidably leads to plastic relaxation, with dislocations negatively affecting the material quality (for example, defective heterointerfaces are electrically active, see Ref. 11 for Ge/Si heterosystems). A multitude of techniques have been developed to reduce threading dislocations (TDs), unimportant for mismatch relaxation but necessarily associated with misfit dislocations (MDs). Notice that while reduction of TDs does not necessarily imply deviating from an ideal planar structure,[12] the density of MDs can be lowered only by adding, at least during some initial stages of growth, further degrees of freedom for strain relaxation, e.g., by enhancing the surface/volume ratio. This can be achieved if a deposition process allowing for selective, laterally unconstrained growth on top of pillars/mesas,[13–17] is designed.

For the Ge/Si(001) system, on which we shall focus our attention, almost ideal vertical growth of Ge on Si pillars has been recently demonstrated.[18] Still, typical pillar dimensions exceeded 1 μm, thus inducing filmlike plastic relaxation of the strain.[17]

Our first attempts to obtain MD-free structures following this strategy were unsuccessful even if Ge selective growth on nanometer sized Si pillars was achieved.[19–21] Subsequently, we have investigated the structural properties of Ge clusters deposited on top of a SiGe thin buffer grown on Si islands and lines fabricated on silicon-on-insulator substrates. By measuring the nanostructure strain by grazing incidence and specular diffraction using laboratory-based x-ray diffraction techniques we demonstrated that the SiGe improves the compliance of the Si compared to direct Ge deposition, prevents plastic relaxation during growth, and allows elastic relaxation before Ge is deposited on top.[22,23]

In this paper we present a further step forward of our studies, by investigating the selective area growth of Ge nanostructures on Si(001) mesas (i.e., low aspect-ratio pillars). Upon reporting clear experimental and theoretical evidence we will show that a suitable deposition process can be exploited to achieve elastic-only relaxation in Ge/Si nanostructures with a lateral size of 100 nm, leading to a local Ge thickness well beyond the classical planar-heteroepitaxy limit.

II. EXPERIMENTS: GROWTH AND TEM CHARACTERIZATION

Silicon nanomesas were fabricated on 200-mm-SOI wafers featuring a 29-nm-thick Si(001) top layer (TOPSI) and 145-nm SiO_2 buried oxide layer. A 2-nm-thick wet silicon oxide and 21-nm-thick Si_3N_4 layers were used as a hard mask for lithographic structuring and subsequent dry etching. We achieved a two-dimensional pattern of Si mesas with 360 nm periodicity. The sidewalls of the Si mesas were cleaned by growth and removal of a 10-nm-thick SiO_2 sacrificial layer. After nitride removal and final cleaning, Si cylindrical mesas 100-nm wide and 27-nm thick were achieved on top of 40-nm-thick SiO_2 mesas. After an additional HF-last cleaning, the samples were loaded in the reduced pressure chemical-vapor deposition (RP-CVD) reactor, where they underwent a short prebake in H_2 atmosphere at 850 °C. Subsequently, Ge was deposited from high purity germane either directly on the Si nanoislands using a two-step process, with a Ge seed layer grown at 300 °C followed by the Ge growth process at 550 °C,[15] or directly at 550 °C on a thin $Si_{0.5}Ge_{0.5}$ buffer layer (SiGe buffer in the following) previously deposited at 600 °C. The Ge content $x = 0.5$ was chosen to maximize the strain partitioning between Si nanoislands and Ge. The samples were investigated by (scanning) transmission electron microscopy ((S)TEM) and energy-dispersive x-ray spectroscopy (EDX) using a FEI Tecnai Osiris instrument operated at 200 kV. STEM images were recorded using bright field (BF) and high-angle annular dark field (HAADF) detectors. Dislocation analysis was performed in TEM mode using a weak-beam dark field (WBDF) technique.

In Fig. 1 we show plane-view TEM micrographs of Ge/Si nanostructures, obtained in (a) BF and (b) and (c) WBDF. First of all, we notice that, at variance with Ref. 18, nanostructures also display significant lateral growth. The abundance of exposed surface could entail enhanced elastic relaxation as compared to flat films. However, misfit dislocations (marked by white arrows) are clearly visible, pointing in crystallographic [110] and [1$\bar{1}$0] direction. The cross-section micrograph [Fig. 1(d)] confirms that misfit dislocations are located at the interface between Si nanoisland and deposited Ge. An interesting finding is that the shape of the Si islands, originally a disk 100 nm in diameter and 27-nm thick, has significantly changed during the Ge deposition. We have verified that this change is not induced by the pre epicleaning performed in H_2 atmosphere.[23]

As it will be clarified later, the Si island top region is highly tensile stressed by the Ge nanostructure owing to the compliance effect. In turn, the stress is responsible for a strain-driven enhanced mobility of the Si atoms in the islands,[24,25] leading to a reshaping of the island itself toward a higher aspect ratio structure, this allowing for a more effective elastic relaxation.

The scenario observed in samples featuring a SiGe buffer is remarkably different. Misfit dislocations are not visible in bright-field or in dark-field plane view TEM micrographs displayed in Figs. 1(e)–1(g). The geometry of the Ge/SiGe/Si nanostructures is clearly illustrated by the cross-section STEM micrographs shown in Fig. 2. Similarly to the Ge/Si case [Fig. 1(d)], the inner core of the nanostructure features a Si island which has, compared to its predeposition shape, a reduced diameter, increased thickness, and shows a weak faceting. The EDX composition mapping in Fig. 2(c) evidences a second inner crystal made of the SiGe buffer layer. The SiGe region display a {111}-faceted lateral surface and features a (001) top facet. A similar shape has been already reported for the selective growth of $Si_{1-x}Ge_x$/Si layer having lower Ge content ($x = 0.2$, see Ref. 26). Finally, a 35-nm-thick Ge outer layer is observed to enclose the SiGe crystal. The outer Ge "crust" preserves the shape featuring low energy facets (e.g., {113} and {111}).[19] In agreement with plane-view micrographs, standard cross-section TEM images ruled out the presence of misfit dislocations.

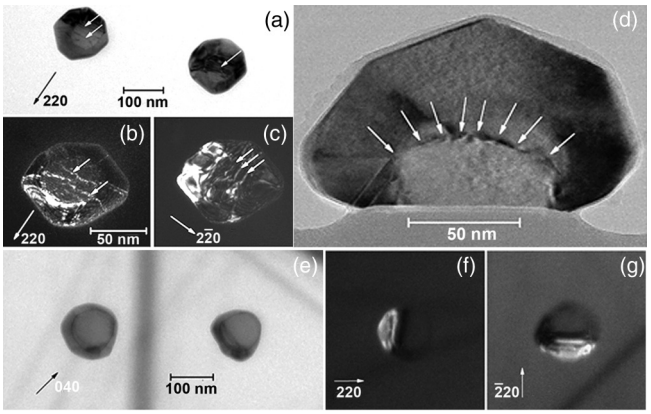

FIG. 1. (a)–(c) Plan-view and (d) cross-section TEM micrographs of Ge/Si nanostructures performed in BF (a) and (d) and WBDF (b) and (c) mode. Misfit dislocations are marked by white arrows. The directions of the incident beam g vectors are also indicated. (e)–(g) Plan-view TEM micrographs Ge/SiGe buffer/Si nanostructures performed in BF (e) and WBDF (f) and (g) mode. There are no misfit dislocations detectable.

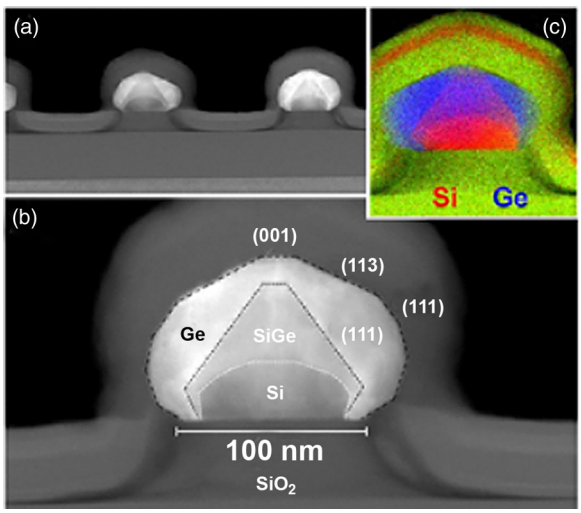

FIG. 2. (Color online) Cross-section STEM HAADF micrograph (a) of two Ge/SiGe buffer/Si nanostructures. Samples are covered by SiO_2 for preparation reasons. (b) The typical faceted geometry. (c) EDX composition mapping (oxygen in green) of the nanostructure in (b).

III. EXPERIMENTS: STRAIN AND COMPOSITION

In order to investigate the lattice strain and the composition of the nanostructures, synchrotron-radiation energy-dispersive grazing incidence x-ray diffraction (SR-GID) was performed at the beamline ID01 of the European Synchrotron Radiation Facility (ESRF). We recall here that, in the spectral region close to the Ge K absorption edge ($E_c = 11.103$ keV), real and imaginary part of the energy dependent correction of the atomic scattering factor strongly vary for Ge, while the scattering factor for Si remains practically constant. This allows for a very sensitive determination of the Ge content in the Ge/SiGe/Si structures independent of the strain state.[27]

Grazing incidence diffraction curves of the in-plane (400) reflection were measured at three different energies 20.5, 5.5, and 2.5 eV below the energy of the Ge K edge with an angle of incidence $\alpha_i = 0.3°$. Results are presented in Fig. 3(a). Experimental data have been fitted using seven Gaussian functions. As an example, the fitting profiles corresponding to the E_c-20.5 eV case are shown in Fig. 3 as short-dashed lines and the relative peak positions are indicated by dash-dotted markers. Here we point out that the curve fitting by seven Gaussian profiles is an approximation, and it does not imply the existence of seven independent crystalline regions with constant Ge content and/or strain value. The composition transitions from Si islands to SiGe buffer and Ge are very likely to be smooth. The peak at 5.4309 Å shows identical intensity for all energies and is accordingly related to pure bulk Si, while the peak close to the bulk Ge lattice parameter shows the strongest differences in intensity for all energies. From additional grazing incidence measurements in off-plane geometry, as well as from laboratory-based specular and grazing incidence diffraction measurements, we know that the highest detectable Ge content in this structure is ~95%. This value and that of bulk Si were used to calibrate the determination of the Ge content vs lattice parameter from pairs of curves at different energy, using the procedure described in Ref. 20, where an averaging over the results of three different combinations of energies was performed for accuracy purpose.

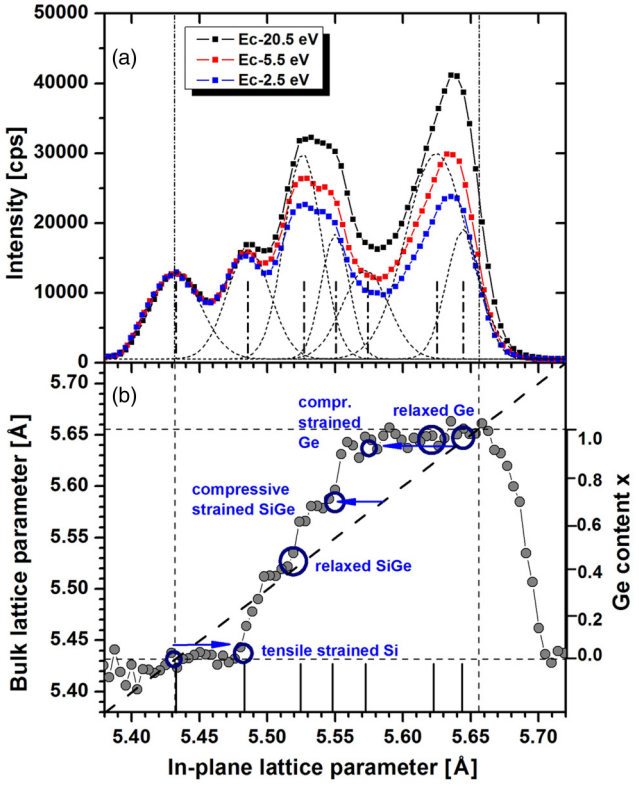

FIG. 3. (Color online) (a) In-plane (400) radial diffraction scans ($\alpha_i = 0.3°$) converted to lattice parameter measured at three different beam energies below the Ge K edge (E_c) of a Ge/SiGe buffer/Si sample; the curve for E_c-20.5 eV is fitted by seven Gaussian curves (short-dashed lines), the corresponding peak positions are indicated by dash-dotted markers, bulk lattice parameters for Si and Ge are marked at 5.4309 and 5.657 Å, respectively (dashed lines). (b) Estimated Ge content and corresponding bulk lattice parameter vs in-plane lattice parameter. Circles indicate by their diameter the area (intensity) of the fitting peaks at the corresponding in-plane position. The diagonal marks the state of full relaxation, while points below this line indicate tensile and above this line compressive strain.

In Fig. 3(b) we show the Ge content as obtained from an analysis of the energy-depending scattering factors of Ge and Si, a method that is completely independent of any strain measurement. From this Ge content it is possible to calculate the corresponding bulk lattice parameter according to Dismukes's quadratic approximation.[28] The experimental data can thus be plotted as bulk lattice parameter vs in-plane lattice parameter, which allows for a direct correlation between strain value and Ge content in the investigated system.

Next to the point corresponding to the SOI substrate Si lattice parameter, a second point at $x = 0$ and in-plane lattice parameter of $a_0 = 5.486$ Å, corresponding to a tensile strain of $\varepsilon \sim 1\%$, can be attributed to the Si nanoislands. The SiGe buffer generates one broad peak (approximated by two Gaussian profiles) with Ge content varying in the $x = 0.4$–0.6 interval and average strain conditions ranging from mainly relaxed to slight compressive strained ($\varepsilon \sim -0.5\%$). A small fraction of the (95%) Ge "crust" is compressively strained, while the major part tends to full relaxation.

IV. MODELING OF COHERENT STRUCTURES

In order to better understand the above experimental findings, we exploited linear elasticity-theory calculations in the isotropic approximation. Elastic constants are reported in Table I.

The geometry of the heteroepitaxial structures was taken from the 2D TEM cross section of Fig. 2(b), while full rotation along the z (001) axis was applied to obtain a 3D geometry. The result of this procedure is displayed in Fig. 4.

TABLE I. Poisson ratio ν and Young modulus E (GPa) for the four materials considered in the elastic calculations.

	ν	E
Ge	0.26	103
Si	0.27	131
$Si_{1-x}Ge_x$	$x\nu_{Ge} + (1-x)\nu_{Si}$	$xE_{Ge} + (1-x)E_{Si}$
SiO_2	0.17	70

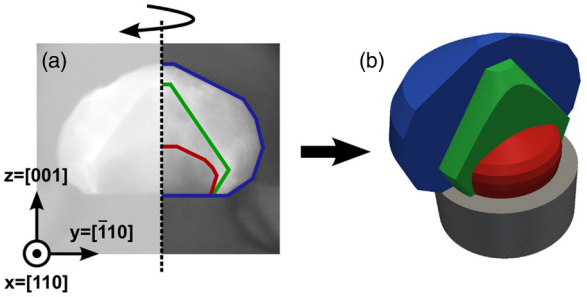

FIG. 4. (Color online) Schematics of the procedure followed to model the geometry of the nanostructures. (a) Actual 2D half-structure cross section on a (110) plane. Lines show the profiles of different domains: inner Si shallow island in red, SiGe steep island in green, and Ge crust in blue. (b) Multiple cross-section plot of the resulting structure after rotation of the 2D half-profile: Colors show different domains as in (a). A simple cylindrical shape is assumed for the oxide mesa.

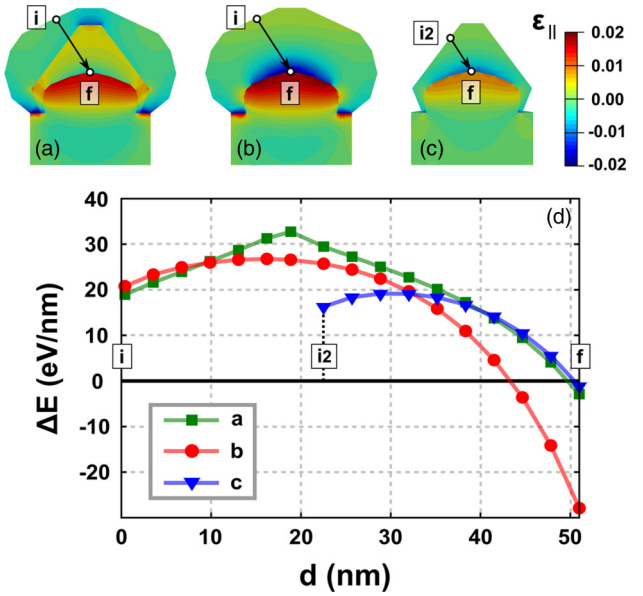

FIG. 5. (Color online) Top three panels: In-plane strain maps of coherent structures, obtained by taking a transversal cross section of the 3D structures perpendicular to the [110] direction. (a) Three-crystal structure ($Si_{0.05}Ge_{0.95}$ crust embedding a steep $Si_{0.5}Ge_{0.5}$ island, embedding a shallow Si island). (b) As in (a), but with the SiGe island replaced by the same material of the external crust. (c) As in (a), but without the Ge crust. We recall that positive strain means tension in the system. For all three cases, the energy difference ΔE between the system with and without a dislocation as a function of the distance from the free surface along the glide plane is reported in (d): the free surface corresponds to point (i) for geometries (a) and (b) and to point ($i2$) for geometry (c), while the upper silicon boundary corresponds to (f) in all the geometries.

The virtually infinite substrate below the nanostructure was simulated by considering a further cylinder (not shown), five times larger than the actual oxide mesa (set to 100 nm, to match experiments) supporting the nanostructure. In actual calculations of the deformation field, all exposed surfaces were treated as free (null normal-stress boundary condition), with the exception of the bottom and of the lateral sides of the substrate. The former was kept fixed; the latter were only allowed to relax along z (roller boundary conditions). We verified that substrate dimensions were large enough to prevent any meaningful, spurious size effect.

In Figs. 5(a)–5(c) results for coherent structures are shown. In particular, Fig. 5(a) reports the in-plane strain $\varepsilon_{||} = 0.5(\varepsilon_{xx} + \varepsilon_{yy})$, as obtained by solving the elastic problem with the Comsol multiphysics finite-element method (FEM) solver, for a structure where the Ge content was tuned based on the above-reported x-rays analysis. On the oxide top, one finds an inner Si-pure shallow island, embedded in a steeper, faceted cluster characterized by a $Si_{0.5}Ge_{0.5}$ alloy, and enclosed by a 95% Ge-rich crust, surrounding the whole nanostructure. The color map of Fig. 5(a) (showing a central section obtained by cutting the 3D nanostructure along the [110] direction) shows that most of the volume occupied by Ge in the crust is relaxed, with the exception of a small region at the nanostructure top, where a compressive strain of $\varepsilon_{||} \sim 1\%$ is found.

These observations are in nice agreement with the experimental measurements of Fig. 3. A strong elastic relaxation had to be expected, as the abundance of free exposed facets allows for the Ge lattice parameter to be recovered. As a result, the Ge layer pulls laterally the inner Si island, causing a remarkable tensile strain of (up to) $\sim$1%, again in agreement with x-ray results (see Fig. 3). We have repeated the calculation by assuming that also the buffer is 95% Ge-rich [Fig. 5(b)], so that the whole structure is now made only of an inner Si island surmounted by a large Ge crust, mimicking the nanostructure shown in Figs. 1(a)–1(d). In the absence of the SiGe buffer, the tensile strain in Si is almost doubled with respect to Fig. 5(a), and the Ge region closer to the inner Si island is now compressed. Notice that both strain maps reveal the SiGe/Si interface to be an ideal region to locate a misfit dislocation, producing compression in the lower region and expansion in the upper one. As previously discussed, experiments without SiGe buffer revealed an array of linear defects at this interface [Fig. 1(d)].

V. MODELING OF STRUCTURES HOSTING MISFIT DISLOCATIONS

The above calculations helped in understanding from the qualitative point of view the role played by the deposition of the buffer layer. The latter was shown to influence elastic relaxation, thus delaying nucleation of misfit dislocation. Here we tackle the problem from a quantitative point of view. We have indeed evaluated the change in energy ΔE produced in the system by inserting a typical 60° misfit dislocation.[29]

In the calculations we considered a single 60°-dislocation misfit segment. In particular, in the coordinate system of the simulation cell (Fig. 4), the following dislocation line ξ and Burgers vector b were chosen $\xi^{60} = (100)$ and $b^{60} = b/2(-1\ 1\ -\sqrt{2})$, where $b = 0.3857$ nm. In the usual coordinate system—$x = (100)$, $y = (010)$, $z = (001)$—this means $\xi^{60} = (110)$ and $b^{60} = b/\sqrt{2}(-1\ 0\ 1)$. This choice for ξ and b defines the unique glide plane of the dislocation, i.e., the $(1\bar{1}1)$ plane. All reported results in terms of energy vs dislocation position were obtained by moving the linear defect along this plane.

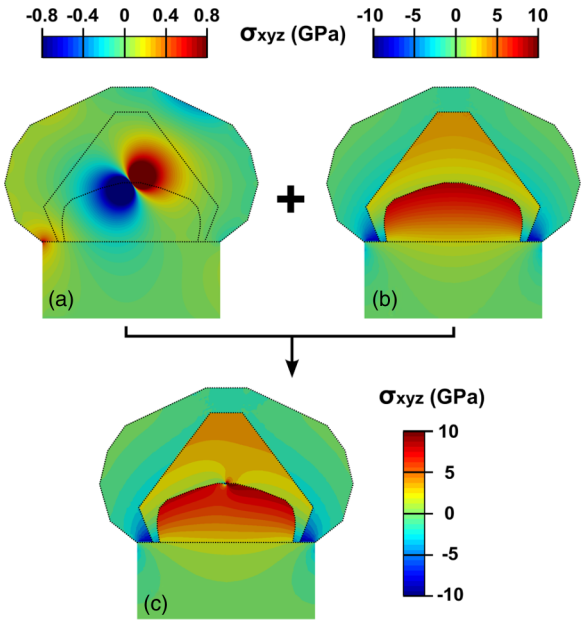

FIG. 6. (Color online) Hydrostatic-stress maps. (a) Hydrostatic stress field for a 60° dislocation calculated in a 2D central section of the full structure. (b) 2D section of the 3D hydrostatic coherent stress field. (c) Superposition of the fields displayed in (a) and (b). The sign of the difference ΔE in elastic energy between (c) and (b) reveals whether or not plastic deformation is thermodynamically favored.

In order to evaluate if plastic deformation is expected in a given nanostructure we proceeded as follows. From both the TEM images of Fig. 1 and the strain maps of Fig. 5, we have individuated the likely positions for misfit-segments positioning in the nanostructures. We then considered the central section of the nanostructures perpendicular to the (straight) dislocation line, and we evaluated its elastic energy (per unit length) $E_{\rm coh}$. Subsequently, we have superimposed to this elastic displacement field that produced by the misfit dislocation, as shown in Fig. 6. The latter was computed by imposing the analytical expression for the stress produced by a bulk 60° dislocation[30] as an eigenstress σ_0 into the same geometrical domain, and by solving the elastic problem (with no additional loads) by FEM as in Ref. 29. This is fundamental to properly consider the (strong) influence of the nanostructure free surfaces on the dislocation field. Divergences at the dislocation core were eliminated as described in Ref. 31. As an additional precaution, we damped the long-range tail of σ_0 by adding to the eigenstress the one of an image dislocation to avoid forcing eigenstresses to nonfree boundaries. Still, we verified that, with our choice for the substrate size, results were unaffected by the additional field. Once the coherent and dislocation-related displacement fields are superimposed, one can calculate $E_{\rm dislo}$, i.e., the elastic energy (per unit length) of the system in the presence of the dislocation. The sign of $\Delta E = E_{\rm coh} - E_{\rm dislo}$ determines whether it is convenient or not to introduce a misfit dislocation, negative values indicating thermodynamically favored plastic relaxation.

In Fig. 5(d) ΔE values are plotted, for the three cases depicted in Figs. 5(a)–5(c), as a function of the distance from the free surface, where dislocations are likely to be nucleated, in the form of half loops.[12] Such distance is computed along the proper glide plane, i.e., along the line connecting the initial (i) and final (f) position indicated in Figs. 5(a)–5(c). In the absence of a SiGe buffer (red curve, circles), the system energy is strongly lowered by the presence of a MD, as this relieves the very high tensile strain which, otherwise, would characterize the Si island. If we take into account the effect of the buffer layer (green curve, boxes), two main differences must be noted. First, the energy gain is dramatically reduced (from -28 to -3.1 eV/nm). Second, at variance with the red curve, the green one becomes negative almost only at the final position ($\sim$1 nm from the interface). Both these observations indicate that, in absence of the SiGe buffer, the system is largely overcritical, while the presence of the buffer layer brings it close to the critical condition for elastic-only relaxation. We point out that, in the absence of the external Ge crust, the inner Si island is under a weak tension [see Fig. 5(c)] and, indeed, the energy gain (blue curve, triangles) is reduced in this case to -1.1 eV/nm, negative ΔE being even more localized close to the final position at the SiGe/Si interface. Therefore, no dislocations are also expected prior to the deposition of the Ge layer,

Summarizing, we can state that in the presence of the SiGe buffer the system appears to be close to the critical condition for dislocation insertion, while being largely overcritical if Ge is deposited without the SiGe "cushion." This conclusion safely justifies the absence of dislocations observed in the TEM images as typically some degree of overcriticality is needed before dislocations actually appear (see, e.g., Ref. 32). Moreover, we believe that our calculations slightly *overestimate* the tendency of the system toward plastic relaxation. A detailed discussion is reported in the next section, yielding also a justification for a discrepancy between theory and experiments for what concerns strain values in the SiGe buffer.

VI. DISCUSSION: DEVIATIONS FROM UNIFORM Ge DISTRIBUTIONS

All theoretical results reported in the previous sections were obtained by assuming uniform compositions (100% Si in the inner island, 50% Ge in the middle one, and 95% Ge in the external crust). Particularly for the 50% Ge buffer region, we are aware that this choice simplifies the actual situation, as measurements revealed possible variations in the Ge (Si) content. Most likely, based on elastic-energy minimization,[33] an accumulation of Ge takes place at the top of the middle layer, while its base should be richer in Si. Such deviations would strengthen our theoretical conclusion on the absence of dislocations. We have indeed repeated the calculations leading to the ΔE curves of Fig. 5(d) (i.e., for a final dislocation position in a region where less than 50% Ge is expected) by varying the buffer-layer island Ge content. It turned out that by lowering the Ge content by only 5% (from 50% to 45%), ΔE becomes positive also at the interface. So, there is a strong indication that by using a more realistic Ge profile within the buffer layer, our conclusion would vary from "system very close to the plasticity onset" to "system below the critical condition for inserting a dislocation," highlighting even better the peculiar resistance towards plastic relaxation of the present nanostructures.

Notice that the above discussed deviation from a uniform composition also helps in explaining the apparent disagreement between theoretical [Fig. 5(a)] and experimental (Fig. 3) results concerning strain values in the SiGe island, above the Si mesa. Experiments yield a slightly negative (i.e., compressive) strain, while FEM calculations, which consider a 50% Ge content, give a slightly tensile strain. Again, more Ge is likely to be present in the top region of the island, enlarging the reference lattice parameters, and therefore canceling the tendency towards tensile strain.

VII. CONCLUSIONS

In this work we have experimentally and theoretically investigated peculiar Ge nanostructures grown on Si(100) mesas with a lateral extension of 100 nm. We have detailed how deposition of Ge onto the mesas leads to a defect free, elastically relaxed nanocrystal provided that an intermediate SiGe buffer is inserted. The buffer produces a morphological change and {111}-faceted island "hosting" an inner Si island are formed providing an ideal support for growing coherent Ge, as demonstrated by the here-proposed modeling of elastic and plastic relaxation. Importantly, the role of such a "3D" buffer layer is very different with respect to the one played by planar ones in standard 2D epitaxy. In the latter case, indeed, buffer layers with a misfit lower than the film/substrate one are used to lower dislocation threading-arms densities.[34] Here it also eliminates misfit segments.

Finally, we notice that deposition of Ge on a flat or pit-patterned Si(001) substrate can lead to coherent nanostructures (3D islands) of similar linear size, self-assembled via the Stranski-Krastanow growth mode.[35] However, pronounced intermixing leads to Si-rich islands.[36] Although the nanostructures presented in this paper display a large Si-rich core, they are surrounded by a fully coherent Ge layer with thickness up to ∼35 nm, i.e., more than one order of magnitude larger than the classical heteroepitaxy critical thickness.[32] In view of possible applications, the difference is substantial.

ACKNOWLEDGMENT

We acknowledge stimulating discussions on nano- and microheteroepitaxy with Leo Miglio.

*capellini@fis.uniroma3.it

[1] H. Dosch and M. H. Van de Voorde (Eds.), GENNESYS, Grand European Initiative on Nanoscience and Nanotechnology Using Neutron- and Synchrotron Radiation Sources, http://www.mpi-stuttgart.mpg.de.

[2] J. Lin, D. A. Antoniadis, and J. A. del Alamo, in *Proceedings of International Electron Device Meeting (IEDM)* (IEEE, Piscataway, NJ, 2012), pp. 757–760.

[3] Y. Q. Wu, M. Xu, R. S. Wang, O. Koybasi, and P. D. Ye, in *Proceedings of International Electron Device Meeting (IEDM)* (IEEE, Piscataway, NJ, 2009), pp. 323–326.

[4] F. Jia, R. Woo, Ch. Shulu, L. Yaocheng, P. B. Griffin, and J. D. Plummer, IEEE Electron Device Lett. **28**, 637 (2007).

[5] C.-T. Chung, C.-W. Chen, J.-C. Lin, C.-C. Wu, C.-H. Chien, and G.-L. Luo, in *Proceedings of International Electron Device Meeting (IEDM)* (IEEE, Piscataway, NJ, 2012), pp. 383–386.

[6] H. Liu, T. Wang, Q. Jiang, R. Hogg, F. Tutu, F. Pozzi, and A. Seeds, Nat. Photon. **5**, 416 (2011).

[7] R. Chen, T.-T. D. Tran, K. W. Ng, W. S. Ko, L. C. Chuang, F. G. Sedgwick, and C. Chang-Hasnain, Nat. Photon. **5**, 170 (2011).

[8] G. Capellini, G. Kozlowski, Y. Yamamoto, M. Lisker, C. Wenger, G. Niu, P. Zaumseil, B. Tillack, A. Ghrib, M. de Kersauson, M. El Kurdi, P. Boucaud, and T. Schroeder, J. Appl. Phys. **113**, 013513 (2013).

[9] M. J. Süess, R. Geiger, R. A. Minamisawa, G. Schiefler, J. Frigerio, D. Chrastina, G. Isella, R. Spolanek, J. Faist, and H. Sigg, Nat. Photon. **7**, 466 (2013).

[10] Ch. M. Lieber, MRS Bull. **36**, 1052 (2011).

[11] R. Peibst, E. P. Rugeramigabo, and K. R. Hofmann, J. Appl. Phys. **112**, 124502 (2012).

[12] E. A. Fitzgerald, Mats. Sci. Rep. **7**, 87 (1991).

[13] S. Luryi and E. Suhir, Appl. Phys. Lett. **49**, 140 (1986).

[14] A. Fischer, H. Kühne, G. Lippert, H. Richter, and B. Tillack, Phys. Status Solidi A **171**, 465 (1998).

[15] D. Zubia and S. D. Hersee, J. Appl. Phys. **85**, 6492 (1999).

[16] D. Zubia, S. H. Zaidi, S. D. Hersee, and S. R. J. Brueck, J. Vac. Sci. Technol. B **18**, 3514 (2000).

[17] H. Xe, P. Lu, Z. Yu, Y. Song, D. Wang, and S. Wang, Nano Lett. **9**, 1921 (2009).

[18] C. V. Falub, H. von Känel, F. Isa, R. Bergamaschini, A. Marzegalli, D. Chrastina, G. Isella, E. Müller, P. Niedermann, and L. Miglio, Science **335**, 1330 (2012).

[19] G. Kozlowski, Y. Yamamoto, J. Bauer, M. A. Schubert, B. Dietrich, B. Tillack, and T. Schroeder, J. Appl. Phys. **110**, 053509 (2011).

[20] P. Zaumseil, G. Kozlowski, Y. Yamamoto, J. Bauer, M. A. Schubert, T. U. Schülli, B. Tillack, and T. Schroeder, J. Appl. Phys. **112**, 043506 (2012).

[21] G. Kozlowski, P. Zaumseil, M. A. Schubert, Y. Yamamoto, J. Bauer, T. U. Schülli, B. Tillack, and T. Schroeder, Nanotechnology **23**, 115704 (2012).

[22] P. Zaumseil, G. Kozlowski, Y. Yamamoto, M. A. Schubert, and T. Schroeder, J. Appl. Cryst. **46**, 868 (2013).

[23] P. Zaumseil, Y. Yamamoto, M. A. Schubert, T. Schroeder, and B. Tillack, Thin Solid Films (unpublished).

[24] D. J. Bottomley, Appl. Phys. Lett. **79**, 1060 (2001).

[25] G. Capellini, M. De Seta, F. Evangelisti, V. A. Zinovyev, G. Vastola, F. Montalenti, and L. Miglio, Phys. Rev. Lett. **96**, 106102 (2006).

[26] L. Vescan, T. Stoica, and E. Sutter, Appl. Phys. A **87**, 485 (2007).

[27] T. U. Schülli, J. Stangl, Z. Zhong, R. T. Lechner, M. Sztucki, T. H. Metzger, and G. Bauer, Phys. Rev. Lett. **90**, 066105 (2003).

[28] J. P. Dismukes, L. Ekstrom, and R. I. Paff, J. Phys. Chem. **68**, 3021 (1964).

[29] R. Gatti, A. Marzegalli, V. A. Zinovyev, F. Montalenti, and L. Miglio, Phys. Rev. B **78**, 184104 (2008).

[30] J. P. Hirth and J. Lothe, *Theory of Dislocations* (Wiley, Hoboken, NJ, 1982).

[31] W. Cai, A. Arsenlis, C. Weinberger, and V. Bulatov, J. Mech. Phys. Solids **54**, 561 (2006).

[32]J. W. Matthews and A. E. Blakeslee, J. Cryst. Growth **27**, 118 (1974).
[33]R. Gatti, F. Uhlik, and F. Montalenti, New J. Phys **10**, 083039 (2008).
[34]A. N. Larsen, Mater. Sci. Semicond. Process. **9**, 454 (2006).
[35]F. Boioli, R. Gatti, M. Grydlik, M. Brehm, F. Montalenti, and L. Miglio, Appl. Phys. Lett. **99**, 033106 (2011).
[36]G. Capellini, M. De Seta, and F. Evangelisti, Appl. Phys. Lett. **78**, 303 (2001).